Novel Soluble Sulfonyl-Containing Conjugated Polymers as Highly Efficient Photocatalysts for CO_2 Reduction Reaction

Cai Cheng-Wei[a†], Kuang-Hao Cheng[a,b†], Palraj Ranganathan[a†], Kuei-Jhong Lin[e], Ching-I Huang[c], Kun-Han Lin[e], Jyh-Chien Chen[b], Leeyih Wang[a,c,d*]

[a]Center for Condensed Matter Sciences, National Taiwan University, No. 1, Sec. 4, Roosevelt Rd. Taipei 10617, Taiwan.

[b]Department of Materials Science and Engineering, National Taiwan University of Science and Technology, 43, Sec. 4 Keelung Road, Taipei 10607, Taiwan.

[c]Institute of Polymer Science and Engineering, National Taiwan University, Taipei 10617, Taiwan

[d]Center of Atomic Initiative for New Materials, National Taiwan University, Taipei 10617, Taiwan

[e]Department of Chemical Engineering, National Tsing Hua University, 101, Section 2, Kuang-Fu Road, Hsinchu 30044, Taiwan

† Cai Cheng-Wei, Kuang-Hao Cheng and Palraj Ranganathan. Contributed equally to this paper

* Corresponding authors. E-mail: leewang@ntu.edu.tw

S1. Synthesis of Monomers

S1.1. 2,5-Dibromo-3-hexylthiophene 1,1-dioxide (2;3HTO-2Br)

2,5-Dibromo-3-hexylthiophene (**1;** 3HT-2Br) (1.50 g, 4.60 mmol) was weighed into a 100 mL single-neck round-bottom flask containing a magnetic stir bar. To this, 30 mL of dichloromethane was added, followed by 3-chlorobenzoperoxoic acid (2.55 g, 14.78 mmol) as the oxidizing agent. The flask was sealed with a serum stopper and wrapped in aluminum foil to shield it from light, then allowed to react at room temperature for 5 days. After completion, the reaction mixture was extracted with deionized water and chloroform. The organic layer was dried over anhydrous magnesium sulfate, filtered, and concentrated under reduced pressure. The crude product was purified by column chromatography using a hexane/ethyl acetate (2:1) eluent. After solvent removal, a pale yellow oily product was obtained (1.10 g, 66.8% yield).

^{1}H NMR (600 MHz, $CDCl_3$), δ (ppm) = 6.85 (s, 1H), 2.43-2.41 (t, J=7.8 Hz, 2H), 1.57-1.53 (m, 2H), 1.38-1.32 (m, 6H), 0.93-0.91 (t, J=6.0 Hz, 3H).

^{13}C NMR (150 MHz, $CDCl_3$), δ (ppm) = 142.01, 130.80, 119.84, 113.91, 31.36, 30.07, 28.73, 26.15, 22.42, 13.99.

S1.2. 2,8-Dibromodibenzo[b,d]thiophene (4)

Dibenzo[b,d]thiophene (**3**) (4.00 g, 0.02 mol) was dissolved in 50 mL of chloroform in a 100 mL single-neck flask equipped with a magnetic stir bar. Bromine (2.8 mL, 0.05 mol) was added dropwise via a syringe through a feeding funnel. The reaction mixture was stirred at room temperature overnight. Following the reaction, the mixture was quenched with an aqueous NaOH solution. The organic layer was extracted with chloroform, washed with deionized water, and dried over anhydrous magnesium sulfate. After filtration, the solvent was removed under reduced pressure using a rotary evaporator. The crude product was recrystallized from chlorobenzene, yielding 3.24 g of white solid with a 47.4% yield.

^{1}H NMR (600 MHz, $CDCl_3$), δ (ppm) = 8.27-8.26 (d, J=1.8 Hz, 2H), 7.74-7.73 (d, J=8.4 Hz, 2H), 7.62-7.60 (dd, J=1.8 Hz and 8.4 Hz, 2H).

^{13}C NMR (150 MHz, $CDCl_3$), δ (ppm) = 138.63, 136.18, 130.30, 124.72, 124.18, 118.63.

S1.2. 2,8-Dimethoxydibenzo[b,d]thiophene (5)

Compound **4** (3.24 g, 9.47 mmol) was dissolved in 18 mL of toluene and 18 mL of methyl acetate in a 250 mL single-neck flask with a magnetic stir bar. After complete dissolution, CuI

(1.86 g, 4.88 mmol) and 66.3 mL of 30% NaOMe in methanol were added. The mixture was stirred, equipped with a reflux condenser, and heated at 80°C overnight. Following the reaction, the solution was cooled to room temperature and quenched with water. The resulting mixture was extracted with deionized water and chloroform. The organic phase was dried over anhydrous magnesium sulfate, filtered, and concentrated under reduced pressure using a rotary evaporator. The crude product was purified by column chromatography with a hexane (2:1) eluent. After drying, 2.00 g of a white solid was obtained, yielding 86.3%.

^{1}H NMR (600 MHz, $CDCl_3$), δ (ppm) = 7.73-7.72 (d, J=8.4 Hz, 2H), 7.59-7.58 (d, J=2.4 Hz, 2H), 7.12-7.11 (dd, J=2.4 Hz and 8.4 Hz, 2H), 3.98 (s, 6H).
^{13}C NMR (150 MHz, $CDCl_3$), δ (ppm) = 157.55, 136.48, 132.53, 123.61, 115.88, 104.92, 55.75.

S1.4. Dibenzo[b,d]thiophene-2,8-diol (6)

Compound **5** (2.00 g, 8.18 mmol) was added to a 250 mL single-neck flask with a magnetic stir bar. The system was purged with nitrogen and evacuated three times. Dry chloroform (80 mL) was introduced using a double-ended needle, and the mixture was cooled in an ice bath. BBr_3 (1.0 M, 17.0 mL, 17 mmol) was then added dropwise via a syringe. The reaction was stirred in the ice bath for 6 hours, then quenched by pouring 200 mL of methanol and stirring at room temperature overnight. The methanol was removed under reduced pressure, and the residue was extracted with deionized water and ethyl acetate. The organic phase was dried over anhydrous magnesium sulfate, filtered, and concentrated. The crude product was purified by column chromatography with a hexane acetate (2:1) solvent system. After concentration, 1.22 g of pink powder was obtained, yielding 69.0%.

^{1}H NMR (600 MHz, DMSO-D_6), δ (ppm) = 9.57 (s, 2H), 7.72-7.70 (d, J=8.4 Hz, 2H), 7.49-7.48 (d, J=2.4 Hz, 2H), 6.98-6.96 (dd, J=2.4 Hz and 8.4 Hz, 2H).
^{13}C NMR (150 MHz, DMSO-D_6), δ (ppm) = 160.31, 141.39, 134.86, 128.85, 121.69, 112.37.

S1.5. 2,8-Bis(octyloxy)dibenzo[b,d]thiophene (7)

Compound **6** (1.22 g, 5.64 mmol) was dissolved in 40 mL of 4-methyl-2-pentanone in a 250 mL round-bottom flask with a magnetic stirrer. To this solution, 1-bromooctane (2.25 g, 11.65 mmol) and K_2CO_3 (3.00 g, 21.71 mmol) were added, and the mixture was stirred. The flask was equipped with a reflux condenser and heated to 130 °C for 24 hours. After cooling to room temperature, the solvent was removed under reduced pressure using a rotary evaporator. The residue was extracted with DI water and chloroform, and the organic layer was dried over

anhydrous magnesium sulfate. Filtration followed by rotary evaporation yielded a crude product. Purification via column chromatography with a hexane: DCM (2:1) solvent system produced a white powder (1.50 g, 77.8% yield).

^{1}H NMR (600 MHz, $CDCl_3$), δ (ppm) = 7.71-7.70 (d, J=8.4 Hz, 2H), 7.58-7.57 (d, J=2.4 Hz, 2H), 7.11-7.09 (dd, J=2.4 Hz and 8.4 Hz, 2H), 4.12-4.10 (t, J=6.6 Hz, 4H), 1.89-1.85 (m, 4H), 1.54-1.43 (m, 4H), 1.42-1.36 (m, 16H), 0.94-0.91 (t, J=7.2 Hz, 6H).

^{13}C NMR (150 MHz, $CDCl_3$), δ (ppm) = 157.03, 136.53, 132.30, 123.51, 116.25, 105.81, 68.61, 31.84, 29.41, 29.40, 29.27, 26.13, 22.68, 14.11.

S1.6. 2,8-Bis(octyloxy)dibenzo[b,d]thiophene 5,5-dioxide (8)

A total of 2.00 g (5.85 mmol) of Compound **7** was dissolved in 50 mL of glacial acetic acid in a 250 mL round-bottom flask, equipped with a magnetic stir bar. Then, 4.36 mL (55.65 mmol) of 30% hydrogen peroxide (H_2O_2) was added. The mixture was stirred and heated to reflux for 2 hours. After the reaction, the solution was cooled to room temperature and poured into water to quench the reaction. The resulting mixture was filtered using a Büchner funnel, and the solid product was washed multiple times with deionized water. The final white solid was obtained, yielding 2.00 g (71.9%).

^{1}H NMR (600 MHz, $CDCl_3$), δ (ppm) = 7.77-7.72 (d, J=8.4 Hz, 2H), 7.21-7.20 (d, J=2.4 Hz, 2H), 7.00-6.99 (dd, J=2.4 Hz and 8.4 Hz, 2H), 4.10-4.08 (t, J=6.6 Hz, 4H), 1.87-1.84 (m, 4H), 1.52-1.41 (m, 4H), 1.40-1.34 (m, 16H), 0.94-0.91 (t, J=7.2 Hz, 6H).

^{13}C NMR (150 MHz, $CDCl_3$), δ (ppm) = 163.68, 133.72, 130.51, 123.50, 115.80, 107.49, 68.82, 31.79, 29.30, 29.21, 29.05, 25.96, 22.65, 14.09.

S1.7. 3,7-Dibromo-2,8-bis(octyloxy)dibenzo[b,d]thiophene 5,5-dioxide (9; DBTOOC$_8$-2Br)

A 50 mL mixture of acetic acid and 50 mL of chloroform was added to a double-neck flask, ensuring complete dissolution of compound **8**. A reflux condenser and a feed funnel were attached to the flask, and 7.2 mL (0.28 mole) of bromine was slowly introduced using a syringe while the mixture was heated to 70 °C and allowed to react overnight. Upon completion, the solution was cooled to room temperature, and all contents were transferred to a NaOH aqueous solution to quench the reaction. The mixture was then extracted with deionized water and chloroform, collecting the organic layer. Anhydrous magnesium sulfate was added to remove moisture, followed by filtration. The solvent was evaporated using a rotary evaporator to yield

a crude product, which was then recrystallized from methanol to obtain 1.50 g of the final white powder product, corresponding to a yield of 56.2%.

^{1}H NMR (600 MHz, $CDCl_3$), δ (ppm) = 7.94 (s, 2H), 7.10 (s, 2H), 4.21-4.19 (t, J=6.6 Hz, 4H), 1.96-1.93 (m, 4H), 1.59-1.57 (m, 4H), 1.43-1.33 (m, 16H), 0.94-0.91 (t, J=7.2 Hz, 6H).

^{13}C NMR (150 MHz, $CDCl_3$), δ (ppm) = 159.94, 131.96, 130.38, 126.73, 114.54, 104.46, 69.99, 31.79, 29.25, 29.19, 28.92, 25.99, 22.67, 14.10.

S1.2. 2,5-Bis(trimethylstannyl)thiophene (11; T-2tin)

Weigh 1.50 g (6.20 mmol) of 2,5-dibromothiophene (**10**) into a 100 mL single-necked flask containing a magnetic stir bar. Evacuate the system and purge with nitrogen to remove water and oxygen. Add 30 mL of anhydrous THF using a double-ended needle. Transfer 9.8 mL (15.68 mmol) of 1.6 M n-butyllithium into the flask via a feeding funnel and stir at -78°C. After 2 hours, add 19.0 mL (19.0 mmol) of 1.0 M trimethyltin chloride and maintain the reaction at -78°C for an additional hour. Allow the mixture to warm to room temperature and stir overnight. Extract with DI water and chloroform, dry the organic layer over anhydrous magnesium sulfate, filter, and evaporate the solvent. Recrystallize from methanol to obtain 1.50 g of white crystalline product (59.0% yield).

^{1}H NMR (600 MHz, $CDCl_3$), δ (ppm) = 7.40 (s, 2H), 0.39 (s, 18H).

^{13}C NMR (150 MHz, $CDCl_3$), δ (ppm) = 143.03, 135.81, -8.19.

S2. Characterization

The characterization techniques utilized in this study encompass ^{1}H NMR spectroscopy, ^{13}C NMR spectroscopy, cyclic voltammetry, UV-Vis absorption spectroscopy, time-resolved photoluminescence (TR-PL), photocurrent measurements, and electrochemical impedance spectroscopy (EIS). Detailed methodologies and measurement parameters for these techniques have been previously reported in our earlier publications [1]. All catalyst masses were measured with a Denver Instrument TB-215D balance.

S3. Determination of AQY

The external quantum efficiency (EQE) and internal quantum efficiency (AQE) of the polymer catalysts were measured under simulated AM1.5G solar light at one-sun intensity. The irradiated area (A) of the sample was 0.0004 m^2. The values of AQE were calculated according

to the equations:

$$AQY(\%) = \frac{Total\ number\ of\ reacted\ electrons}{Total\ number\ of\ absorbed\ photons} X\ 100\%$$

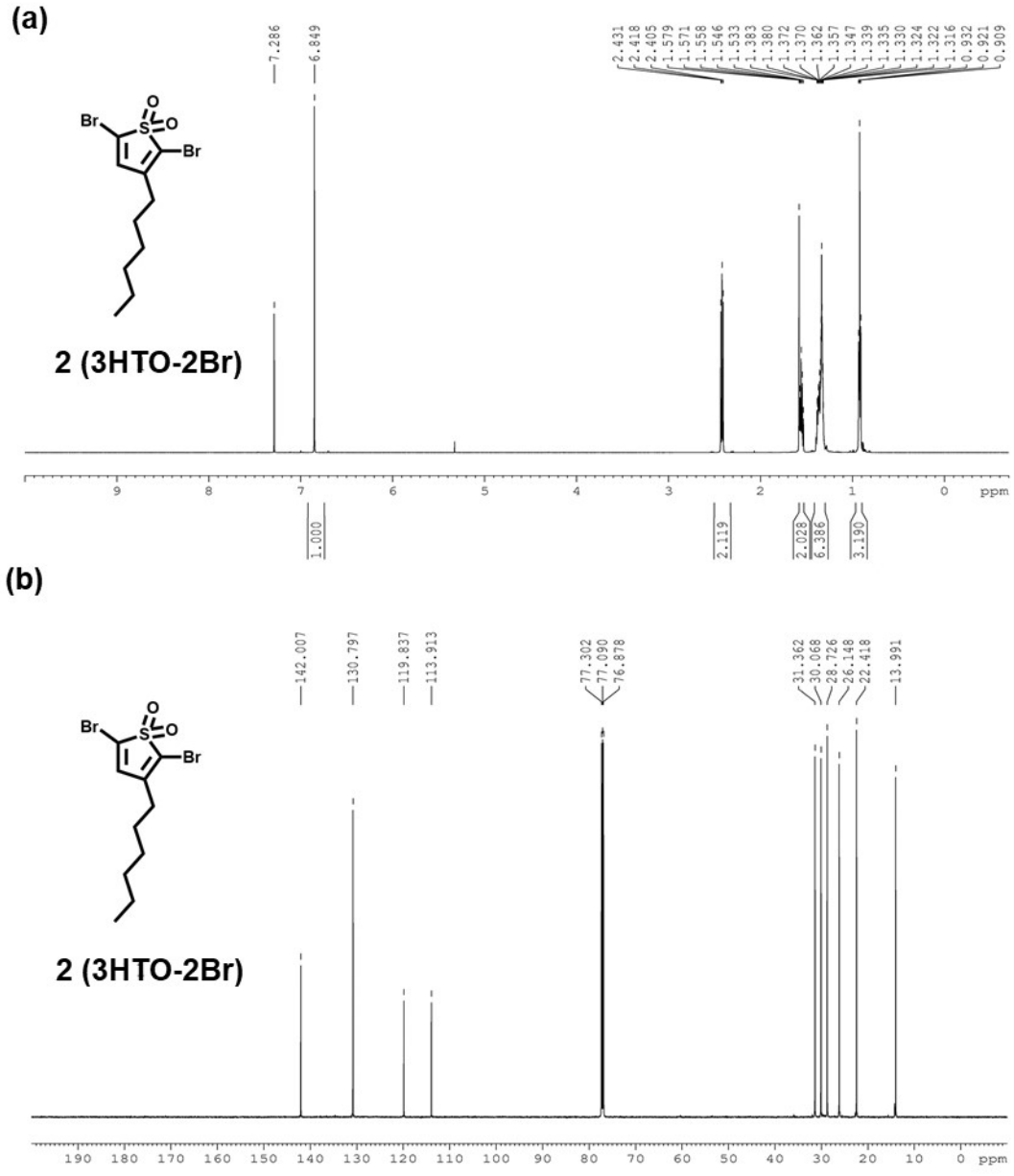

Fig. S1. ^{1}H NMR (a) and ^{13}C NMR (b) spectra of 3HTO-2Br (2).

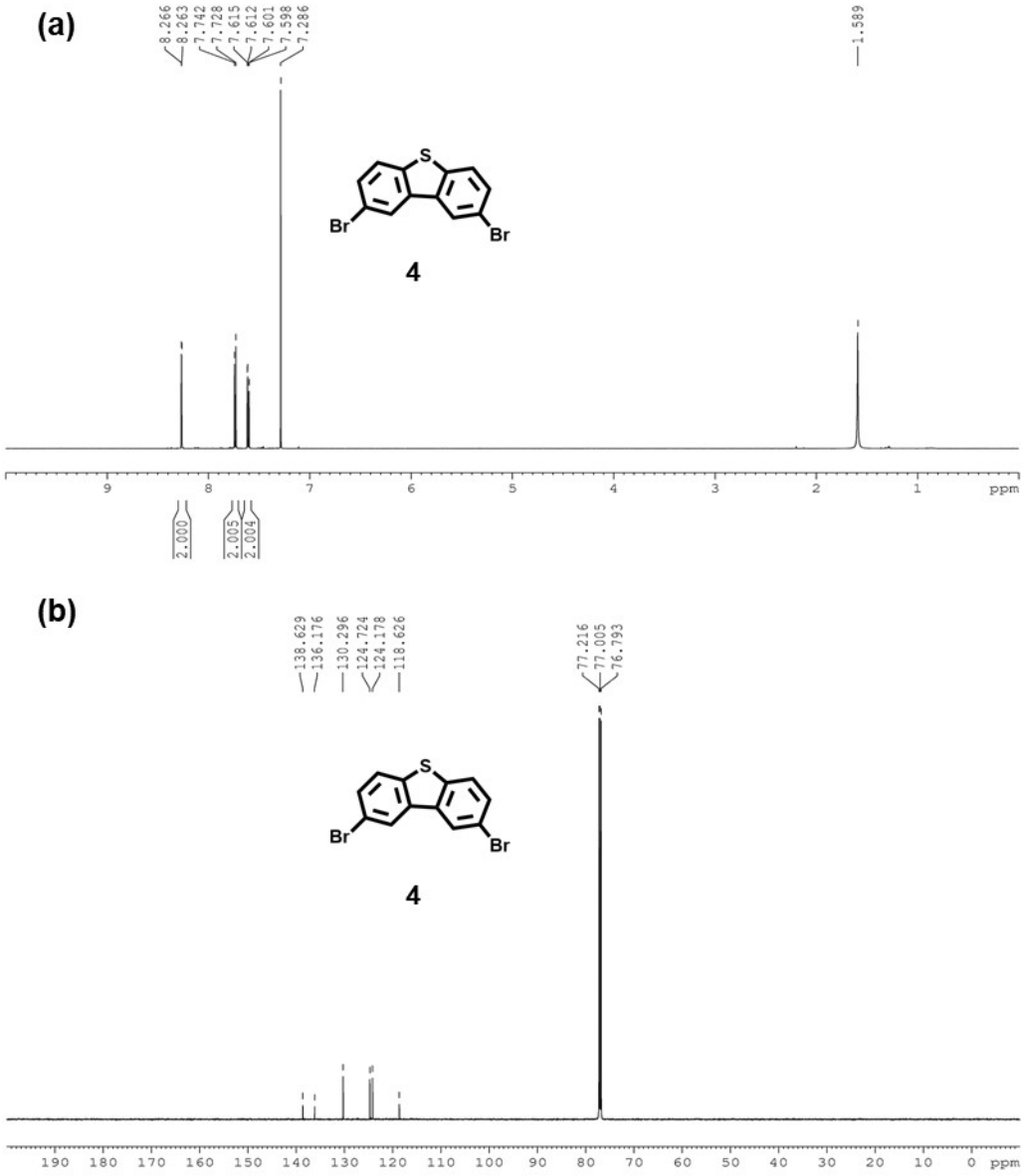

Fig. S2. ^{1}H NMR (a) and ^{13}C NMR (b) spectra of compound **4**.

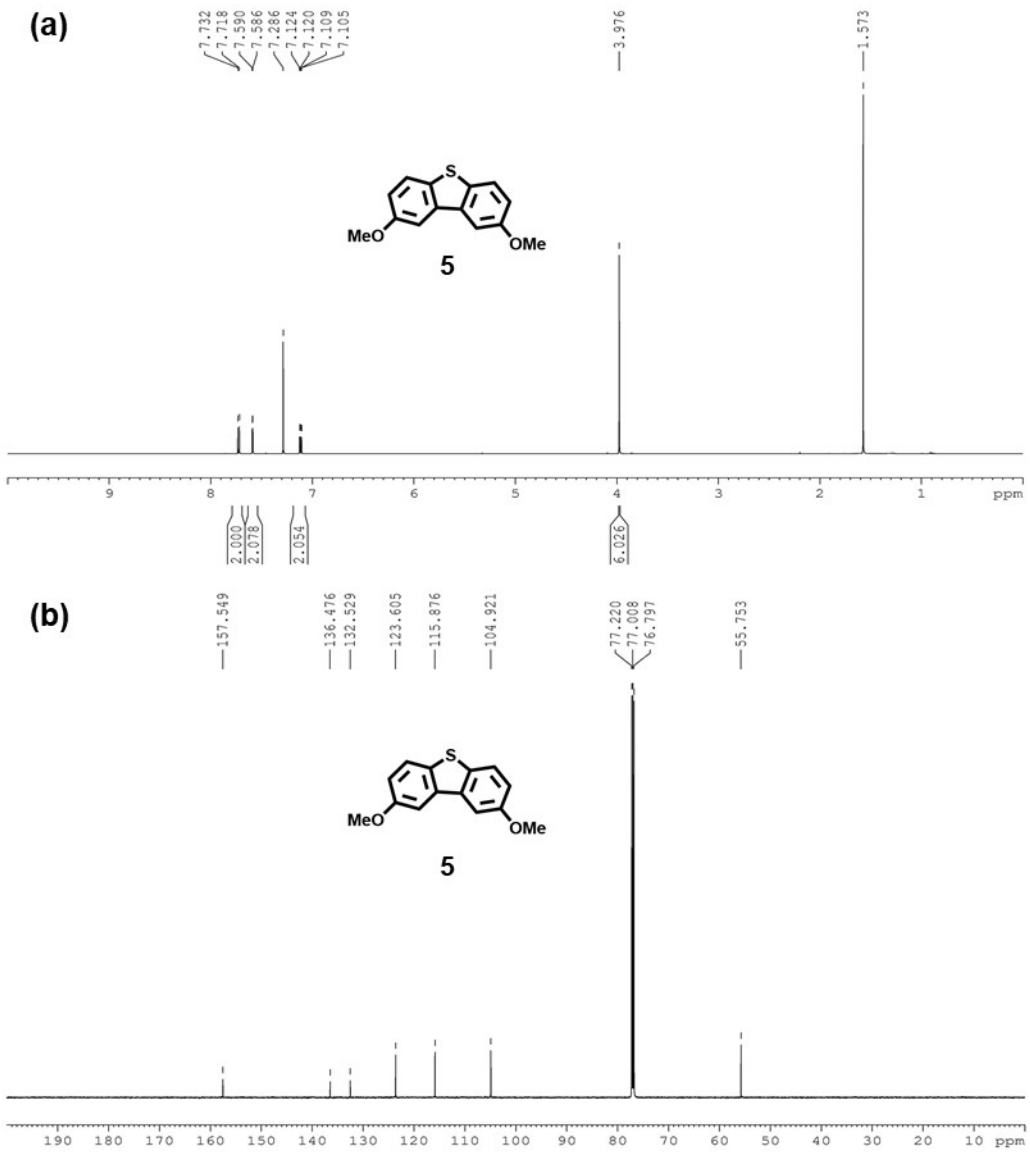

Fig. S3. ^{1}H NMR (a) and ^{13}C NMR (b) spectra of compound **5**.

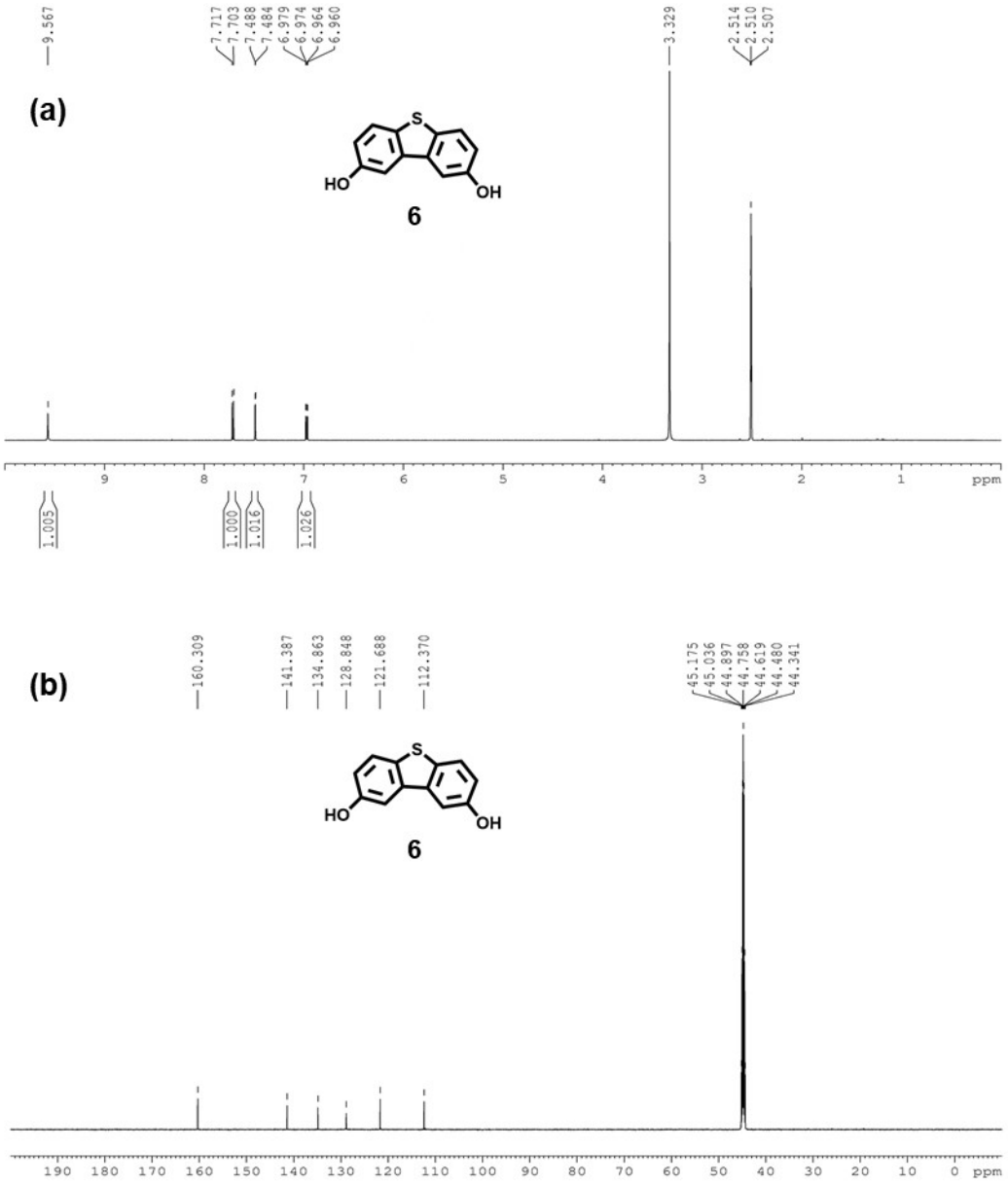

Fig. S4. ^{1}H NMR (a) and ^{13}C NMR (b) spectra of compound **6**.

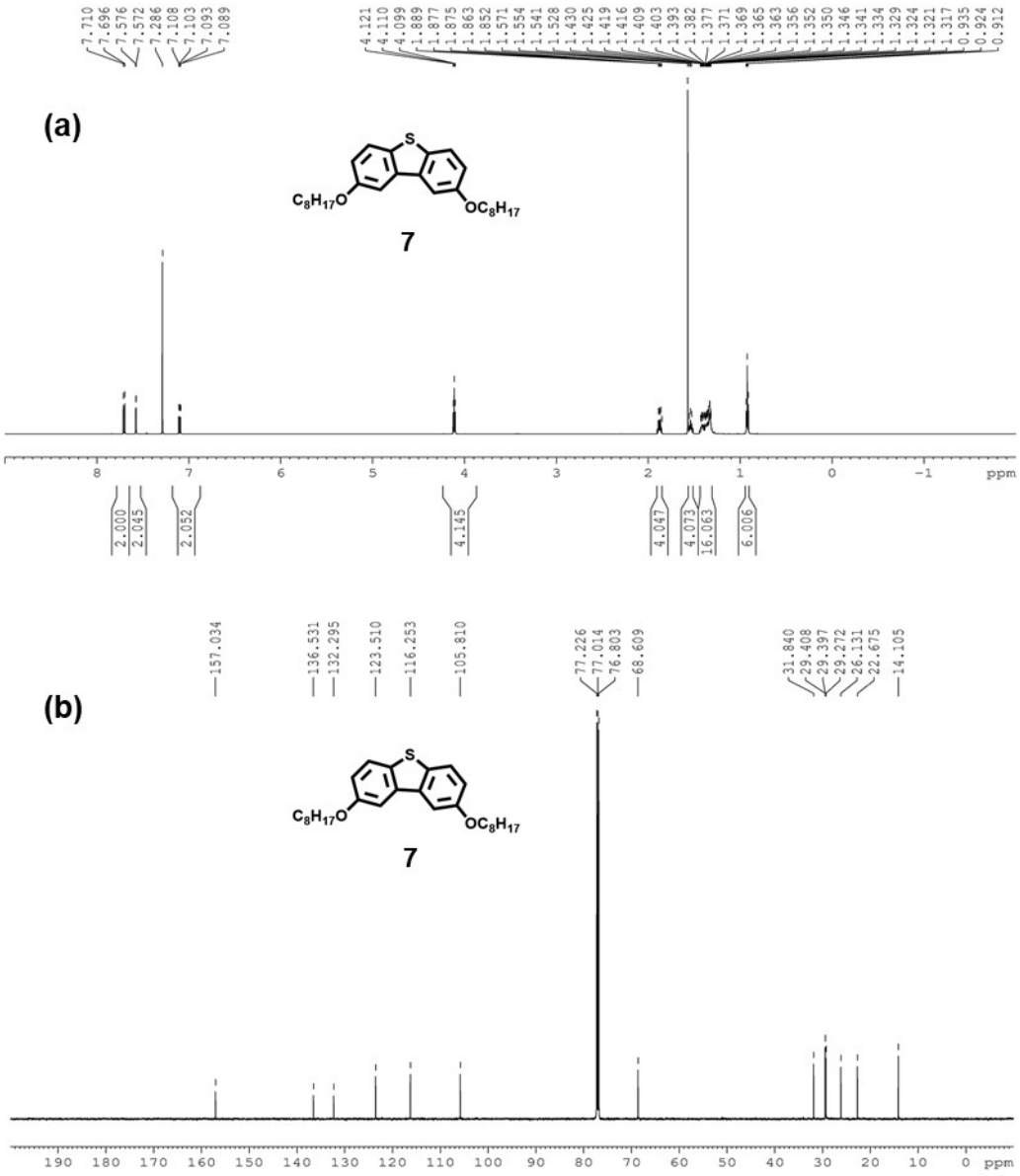

Fig. S5. ^{1}H NMR (a) and ^{13}C NMR (b) spectra of compound **7**.

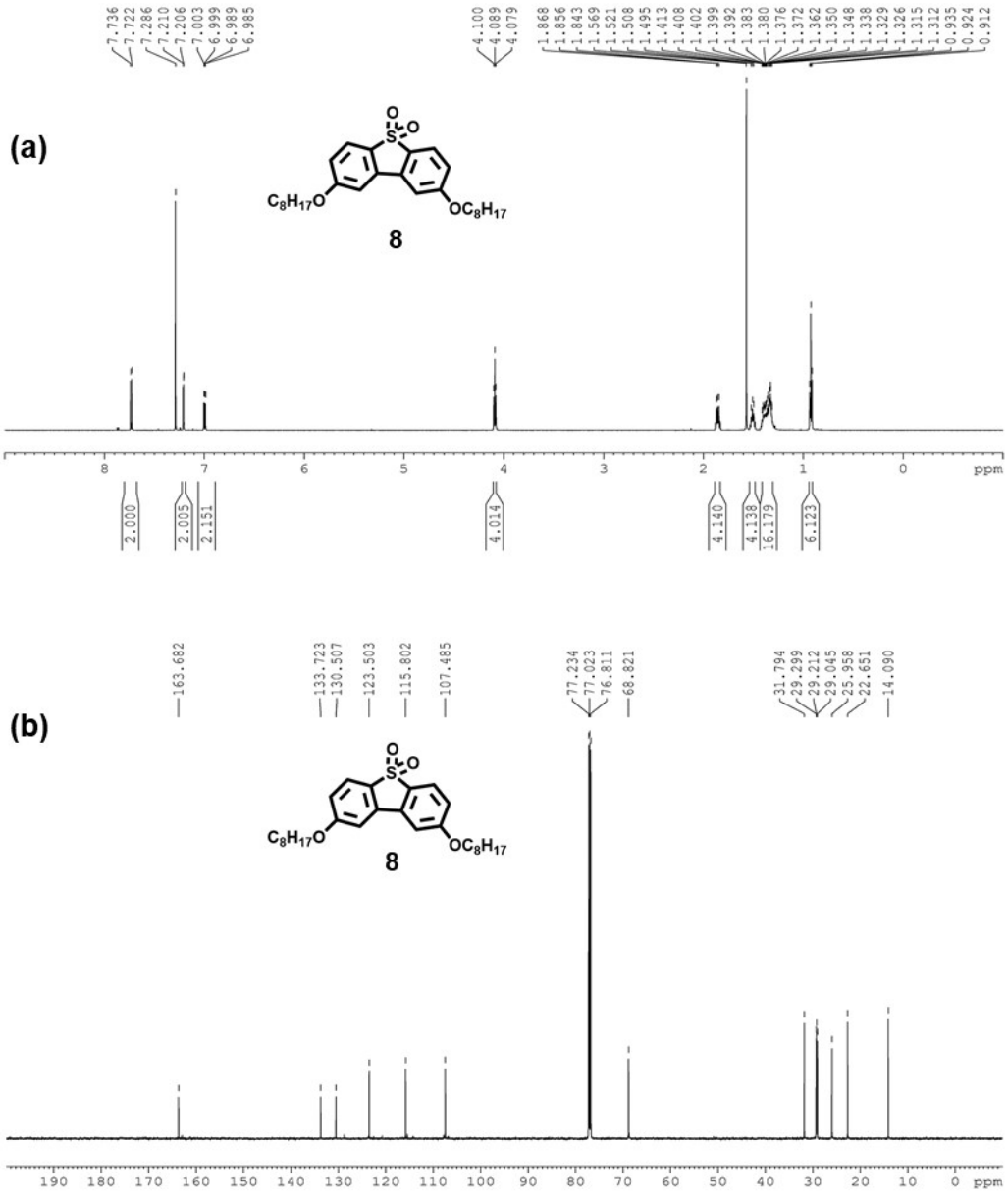

Fig. S6. ^{1}H NMR (a) and ^{13}C NMR (b) spectra of compound **8**.

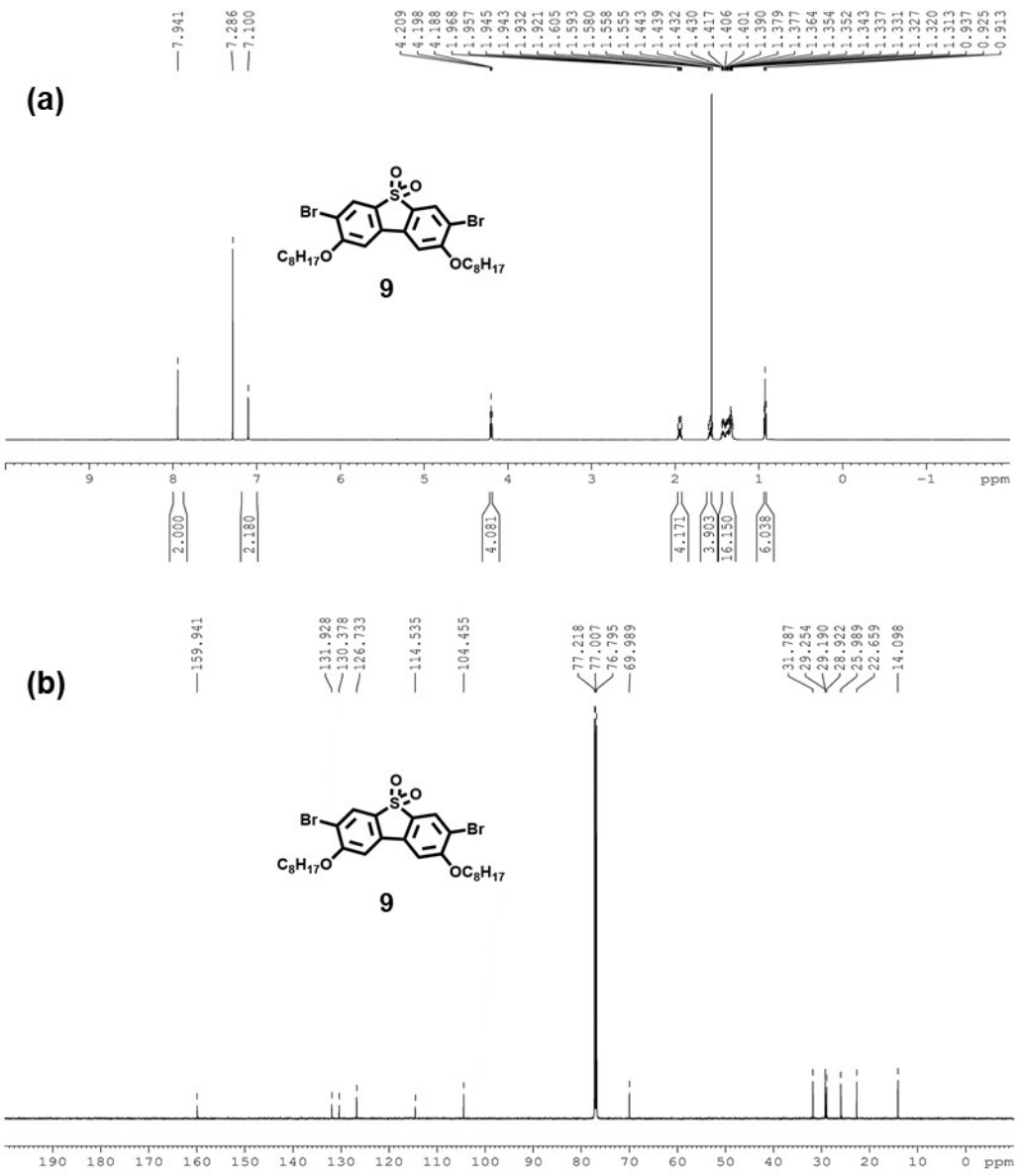

Fig. S7. ^{1}H NMR (a) and ^{13}C NMR (b) spectra of compound **9**.

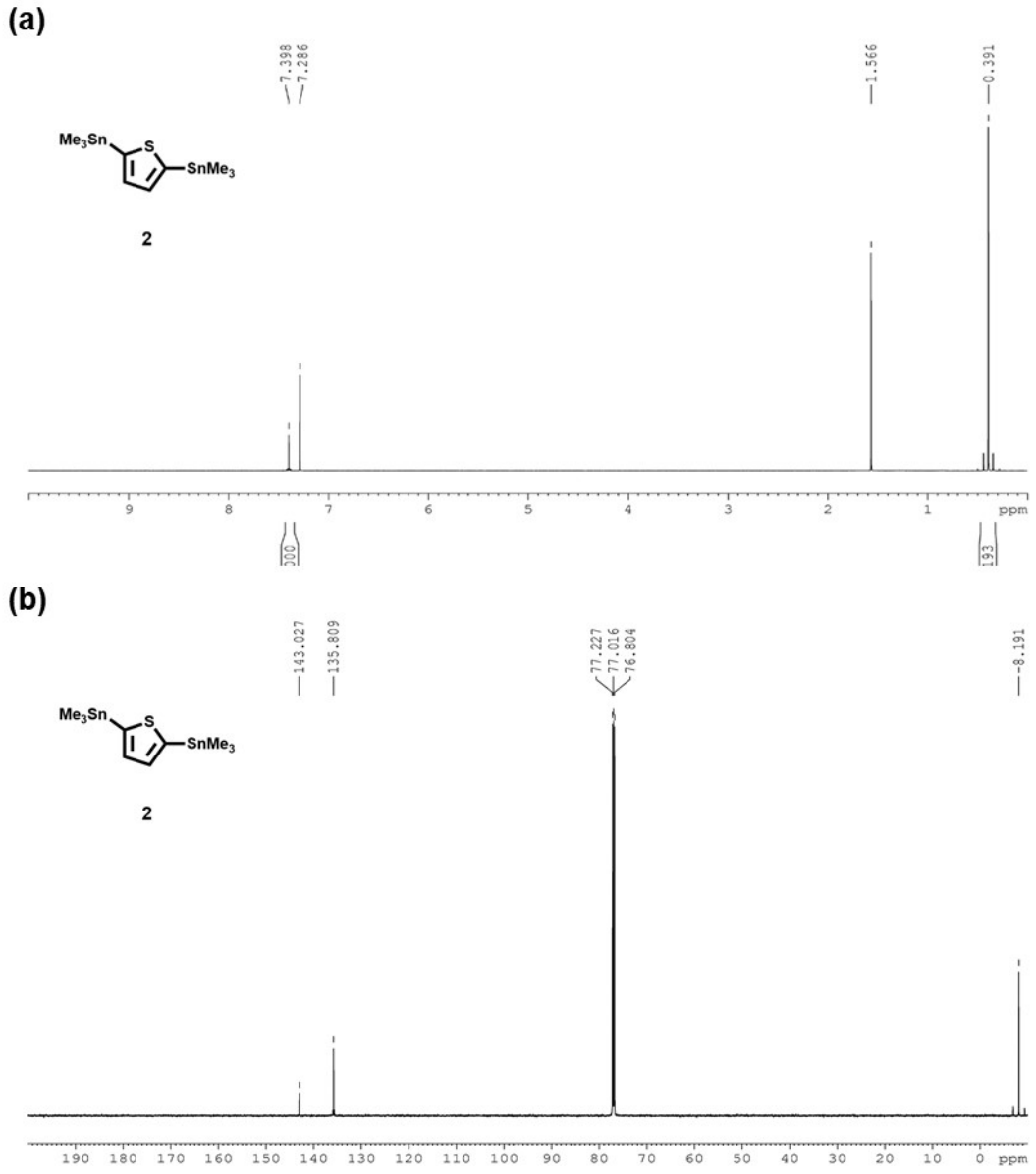

Fig. S8. ^{1}H NMR (a) and ^{13}C NMR (b) spectra of compound **11**.

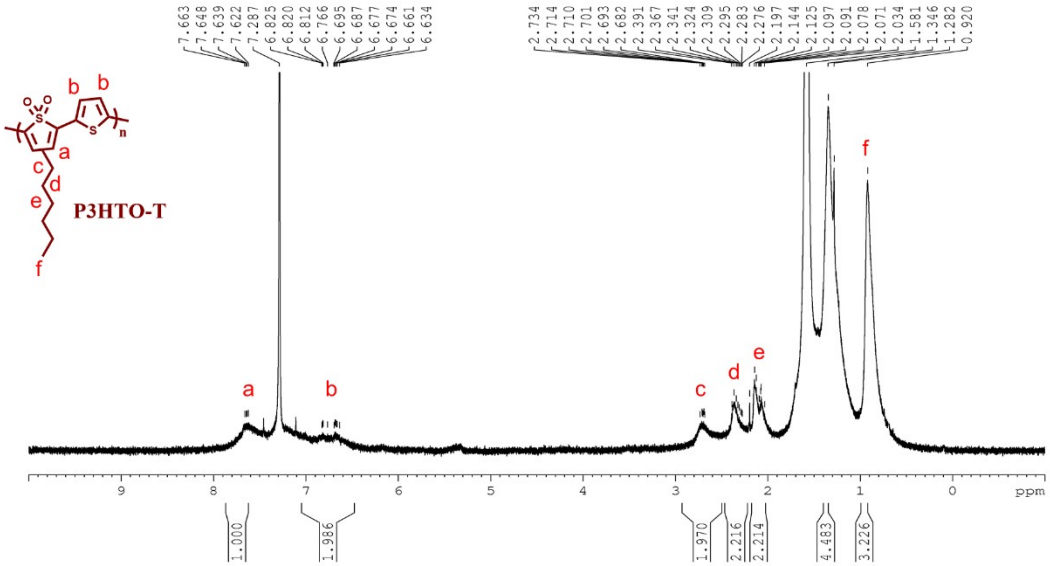

Fig. S9. ^{1}H NMR spectra of P3HTO-T polymer.

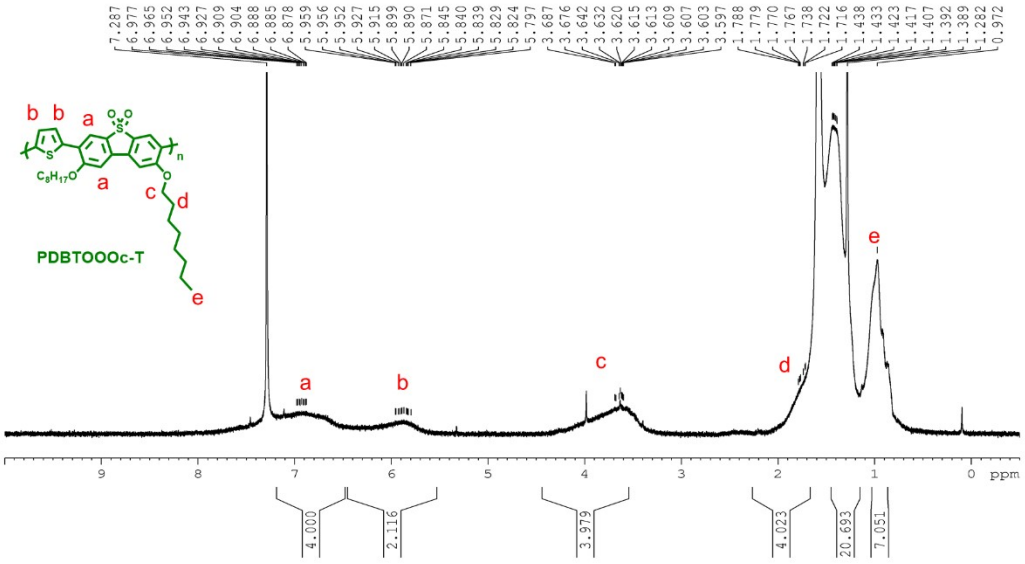

Fig. S10. ^{1}H NMR spectra of PDBTOOC$_8$-T polymer.

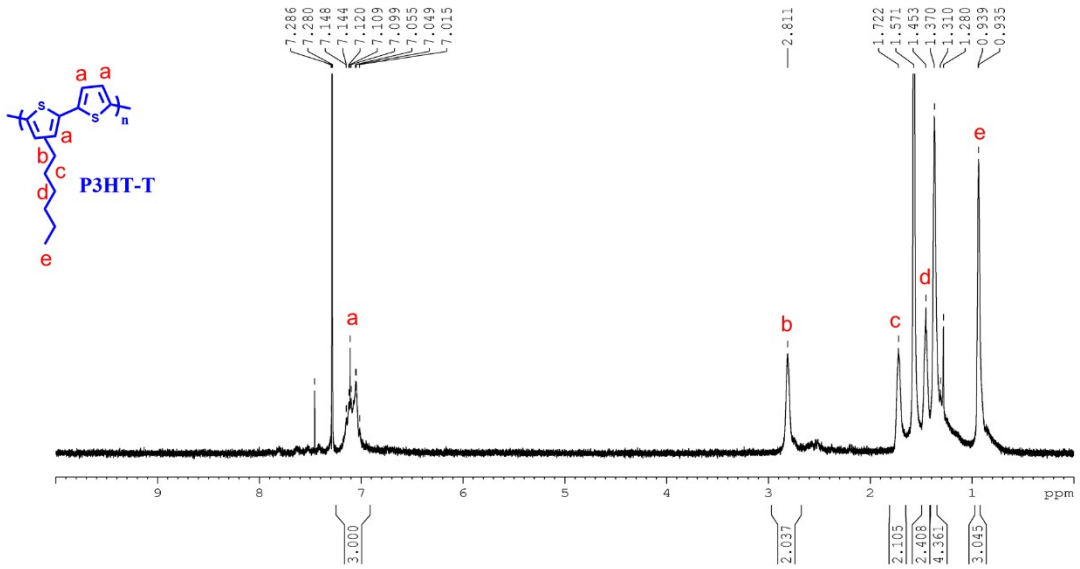

Fig. S11. ^{1}H NMR spectra of P3HT-T polymer.

Table S1. Molecular weights of the synthesized polymers.

Polymers	Mn (kDa)	Mw (kDa)	PDI (Đ)
P3HT-T	6.1	10.7	1.75
P3HTO-T	5.4	9.2	1.70
PDBTOOC$_8$-T	5.4	5.6	1.04

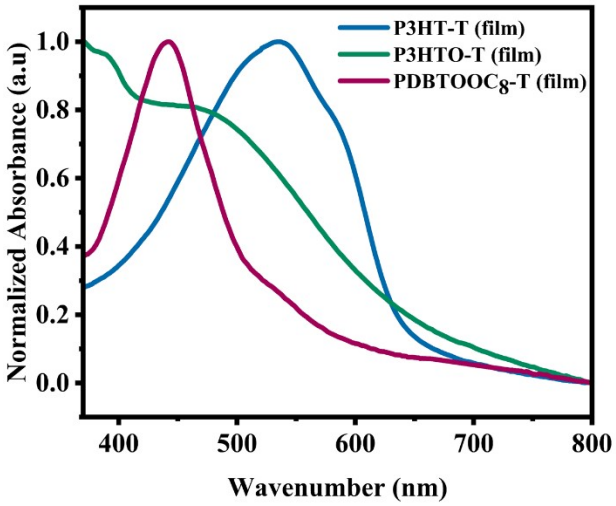

Fig. S12. UV–Vis absorption spectra of P3HT-T, P3HTO-T, and PDBTOOC$_8$-T as spin-coated films.

Table S2. Optical properties and energy levels of P3HT-T, P3HTO-T, and PDBTOOC$_8$-T polymers.

Polymers	$E_{onset}{}^{red}{}_{FC/FC+}$ (V) (vs. Ag/AgCl)	E_{onset}^{red} (V) (vs. Ag/AgCl)	E^{re} (V) (vs Fc/Fc$^+$)	LUMO	HOMO	LUMO (vs. NHE)	E_g	HOMO (vs. NHE)
P3HT-T	0.49	-0.76	-1.25	-3.55	-5.46	-0.95	1.91	0.96
P3HTO-T	0.52	-0.66	-1.18	-3.62	-5.45	-0.88	1.83	0.95
PDBTOOC$_8$-T	0.53	-0.84	-1.37	-3.43	-5.49	-1.07	2.06	0.99

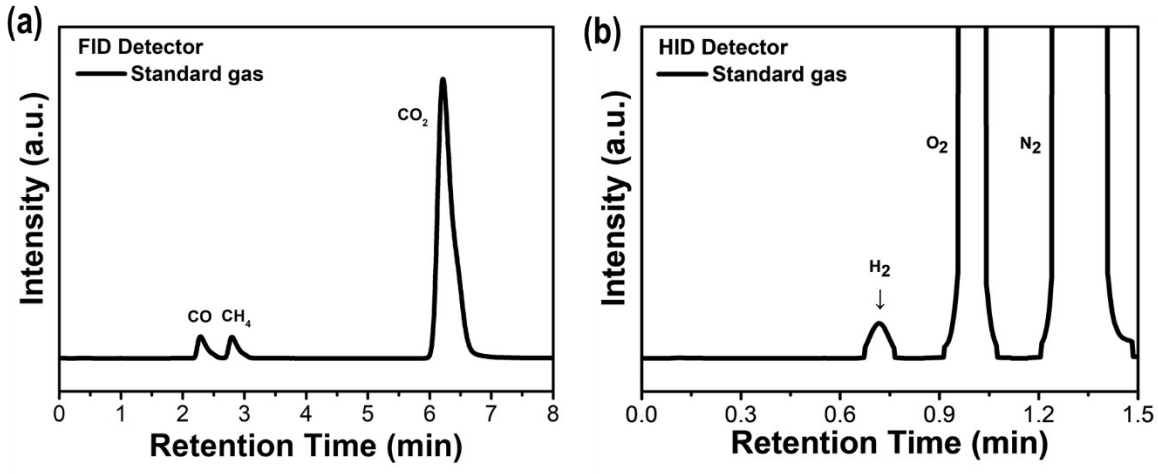

Fig. S13. (a) GC chromatograms of a standard gas mixture containing H_2, CO, and CH_4 detected by (a) FID and (b) HID.

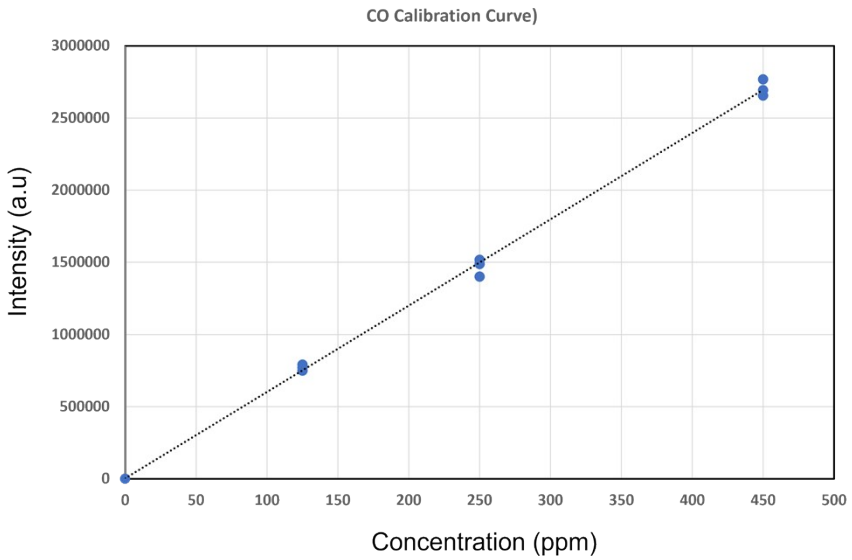

Analyte	Calibration slope (S)	σ (a.u.)	R^2	LOD (ppm)	LOQ (ppm)
CO	6,339.2	21,200	0.9996	11.0	33.4

Fig. S14. Calibration curve of CO by GC-FID detector.

Table S3. Illuminated area and measured CO yield of each photocatalytic run in the glass-substrates system.

Experiment	Catalysts (mg)	Area (CO)	time(h)	CO Yield (umole/g*hr)
	0.20	**11,850**	**3**	**11.4**
	0.19	**12,443**	**3**	**12.6**
P3HT-T	**0.21**	**12,443**	**3**	**11.4**
	0.20	**11,746**	**3**	**11.3**
	0.18	**9,636**	**3**	**10.3**
	0.20	**40,748**	**3**	**39.2**
	0.20	**44,906**	**3**	**43.2**
P3HTO-T	**0.19**	**40,587**	**3**	**41.1**
	0.21	**46,933**	**3**	**43.0**
	0.20	**42,203**	**3**	**40.6**
	0.20	**50,207**	**3**	**48.3**
	0.19	**47,499**	**3**	**48.1**
DBTOOOC8-T	**0.20**	**47,401**	**3**	**45.6**
	0.21	**53,372**	**3**	**48.9**
	0.20	**50,415**	**3**	**48.5**

Table S4. Illuminated area and measured CO yield of each photocatalytic run in the molecular sieves system.

Experiment	lamp	Catalysts (mg)	Area (CO)	time(hr)	CO Yield (umole/g*hr)
		0.20	31,600	18	30.4
		0.19	24,589	18	24.9
P3HT-T	S2	0.21	27,068	18	24.8
		0.20	27,962	18	26.9
		0.18	26,195	18	28.0
		0.20	141,058	18	135.7
		0.20	138,563	18	133.3
P3HTO-T	S1	0.21	149,639	18	137.1
		0.20	134,302	18	129.2
		0.19	134,005	18	135.7
		0.21	271,341	18	248.6
		0.20	264,033	18	254.0
DBTOOOC8-T	s2	0.20	267,254	18	257.1
		0.19	258,830	18	262.1
		0.22	296,954	18	259.7

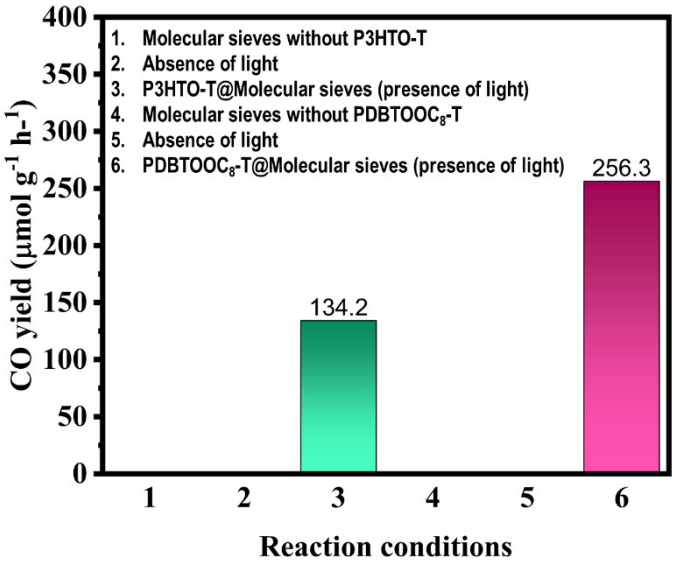

Fig. S15. CO production rates of P3HTO-T and PDBTOOC$_8$-T coated on molecular sieve under different control reaction conditions.

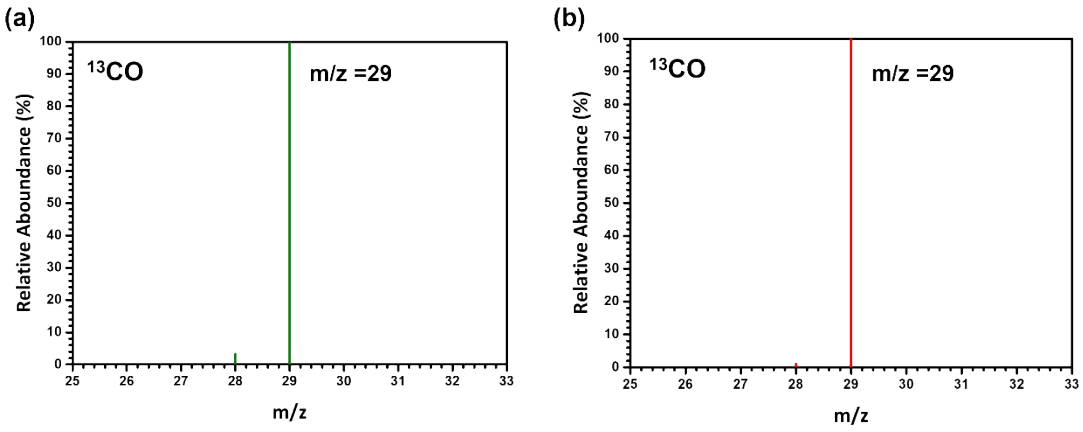

Fig. S16. Mass spectra of products generated from CO_2RR utilizing (a) P3HTO-T and (b) PDBTOOC$_8$-T as catalysts, with $^{13}CO_2$ and as reactants.

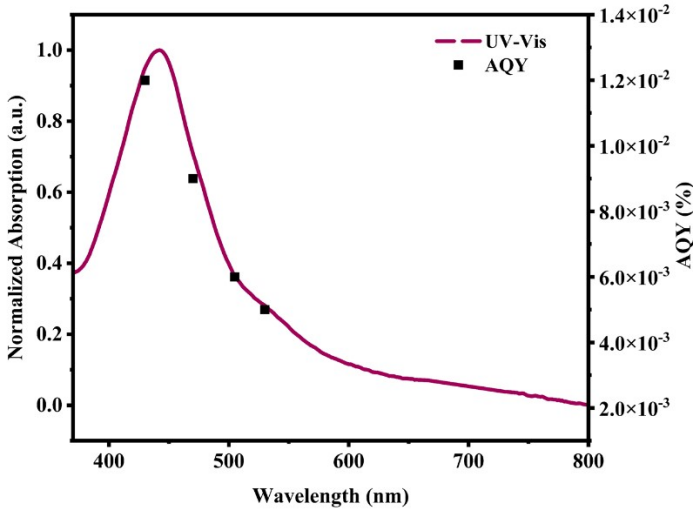

Fig. S17. Wavelength-dependent AQY and UV-vis spectra of PDBTOOC$_8$-T.

Table S5. Comparison of the CO_2 reduction performance of synthesized P3HT-T, P3HTO-T, and PDBTOOC$_8$-T with the organo-catalysts published in the previous literature

Catalyst	Light	Sacrificial agent	CO yield	selectivity	ref

	source				
P3HT-T	AM1.5 solar stimulator	-	27.0 μmol g^{-1} h^{-1}	100	This work
P3HTO-T	AM1.5 solar stimulator	-	134.2 μmol g^{-1} h^{-1}	100	This work
PDBTOOC$_8$-T	AM1.5 solar stimulator	-	256.3 μmol g^{-1} h^{-1}	100	This work
BP-T-LCP	visible-light (λ > 420 nm)		218.9 μmol g^{-1}	100	[S1]
PFT	100 mW cm^{-2} Xe lamp	acetonitrile	231 nmol h^{-1}	-	[S2]
Azo-PZ	500 W Xe lamp	-	92.8 μmol g^{-1} h^{-1}	-	[S3]
PNDI-BP	AM1.5 solar stimulator	TEA	214.8 (CO)/(CH_4)161.4 μmol g^{-1}	-	[S4]
TFPT-DAB	300 W Xe lamp	TEOA	178.45 (CO) μmol g^{-1} h^{-1}	100	[S5]
TAT-PYTA	450 W Xe lamp	-	77.8 μmol g^{-1} h^{-1}	98	[S6]
D1/A1	300 W Xe lamp	AA	23 (H) μmol h^{-1}	100	[S7]
CN/CTF	300 W Xe lamp	TEOA	771 (CO) μmol g^{-1}	100	[S8]
CP5	220 W Xe lamp	TEOA	47.37 (CO)/0.81 (H_2) (mmol h1 g1)	98.3	[S9]
Re-COF	white light	TEOA	15 (CO) μmol g^{-1} h^{-1}	98	[S10]
N_3-COF	225 W Xe lamp	-	57 (CH_3OH) μmol g^{-1} h^{-1}	100	[S11]
PF-Br	AM1.5 solar stimulator	-	9.18 (CO) μmol g^{-1} h^{-1}	-	[S12]
PTPP-DA	300 W Xe lamp	TEOA	465 (CO)/237 (CH_4) μmol g^{-1} h^{-1}	-	[S13]
DTBT-C_{60}	AM1.5 solar stimulator	-	144 (CO) μmol g^{-1}	100	[S14]
TT-COF	450 W Xe lamp	TEA	6.45 μmol g^{-1} h^{-1}	83	[S15]
PEosinY-1	300 W Xe lamp	-	33 (CO)/2.8 (H_2) μmol h^{-1}	92	[S16]
SAS/Tr-COF	300 W Xe lamp	TEOA	980.3 μmol g^{-1} h^{-1}	96.4	[S17]
CN–CV	300 W Xe lamp	-	4.18 (CO) μmol g^{-1} h^{-1}	100	[S18]
UCN-TP0.06	300 W Xe lamp	TEOA	68.18 (CO) /18.52 (H_2) μmole	-	[S19]
D1/A1	300 W Xe lamp	AA	23 (H) μmol h^{-1}	100	[S20]
pTA-Ph	300-W Xe lamp	-	66 μmol h^{-1} m^{-2}	100	[S21]

Table S6. EIS fitting data of the P3HT-T, P3HTO-T, and PDBTOOC$_8$-T polymers.

Polymers	R_{ct} (Ohm)	CPE_1 (nF)	R_1 (Ohm)	CPE_2 (nF)
P3HT-T	323.0	0.15	753.0	4.3
P3HTO-T	156.9	0.35	795.1	1.5
PDBTOOC$_8$-T	106.5	0.57	459.7	12.25

DFT Calculations

All density functional theory (DFT) calculations were performed using the ORCA 5.0 package[S22]. All geometries were optimized at the PBE0-D3(BJ)/def2-TZVP level of theory, which was also used for molecular orbital (MO) analyses, electrostatic potential (ESP) mapping, and Hirshfeld charge calculations. Gibbs free energy calculations were calculated using a composite method where the single-point energy is computed using the DLPNO-CCSD(T)/def2-TZVP method and the free energy correction is calculated using the rigid-rotor-harmonic-oscillator (RRHO) approximation at the PBE0-D3(BJ)/def2-TZVP level. Further computational details are provided in the Supporting Information.

Conformer Search Calculations

Conformer search was performed using the Amsterdam Modeling Suite (AMS) software[S23] with CREST[S24] as the generation method. A machine-learning potential (MLP) based on the AIMNet2-wB97MD3 model was employed to sample the CO_2 adsorption configurations.[S25]

Conformer search

Conformer searches were performed based on monomer models (3HT, 3HTO, and DBTOOC) using the Amsterdam Modeling Suite (AMS).[S26] To sample CO_2 adsorption conformations, we utilized CREST[S27] protocol with machine-learning potential (AIMNet2-wB97MD3).[S28] Sampling was confined by a harmonic wall with an effective radius of 8.3 Å, yielding ~900 conformers per system. For analysis, we measured distances between CO_2 and key functional sites—the thiophene sulfurs (S1, S2), octyloxy oxygens (O1, O2), and sulfone oxygens (SO_2)—and classified each monomer–CO_2 complex by the nearest functional group. All structures were visualized using the VIAMD software.[S29]

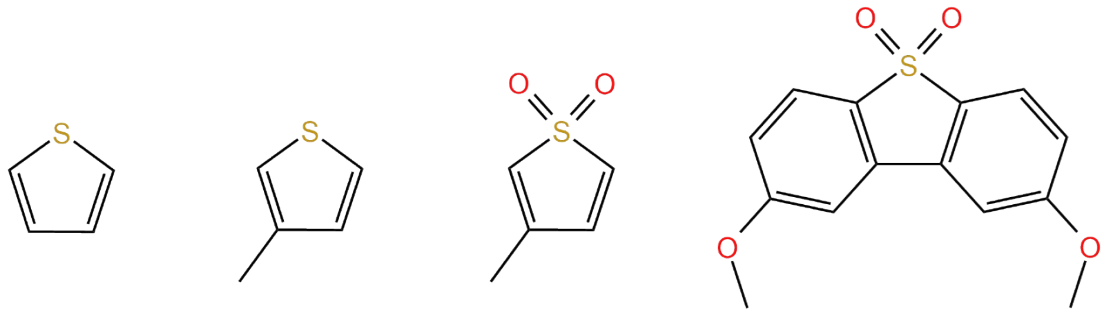

Fig. S18. The molecular structures of the fundamental building blocks (T, 3HT, 3HTO, and DBTOOC).

Gibbs free energy diagram

To identify potential catalytic sites, we constructed Gibbs free-energy diagrams for the following CO_2-to-CO pathway on each polymer (based on monomer model M):[30]

$$M + CO_2 \rightarrow M\cdots CO_2 \quad \Delta G_1$$

$$M\cdots CO_2 + H^+ + e^- \rightarrow MCOOH \quad \Delta G_2$$

$$MCOOH + H^+ + e^- \rightarrow M\cdots CO + H_2O \quad \Delta G_3$$

$$M\cdots CO \rightarrow M + CO \quad \Delta G_4$$

where $\cdots$ in $M\cdots CO_2$ and $M\cdots CO$ means physical adsorption. Gibbs free energies for each molecular species were obtained with a composite protocol: DLPNO-CCSD(T)/def2-TZVP single-point energies on PBE0-D3(BJ)/def2-TZVP geometries, with free-energy corrections from the rigid-rotor–harmonic-oscillator (RRHO) approximation at the same DFT level.

The chemical potentials of proton and electron were treated using the computational hydrogen electrode[31] as shown below.

$$\mu_{H^+} + \mu_{e^-} = \frac{1}{2}G^0_{H_2} + k_B T ln(a^+) - eU$$

where $G^0_{H_2}$ is the Gibbs free energy of H_2 at standard state, k_B is the Boltzmann constant, T the temperature, and a^+ the proton activity (where we used pH = 7). We considered two electrochemical potentials: (i) $U = 0$ and (ii) $U = E^*_{ox}$, representing photoexcited conditions with increased electron reducing power. The excited-state oxidation potential was estimated as

$$E^*_{ox} = -\frac{4.50 - (IE - E_{0,0})\ (in\ eV)}{e}$$

where IE is the ionization energy (approximated from the minus experimental HOMO level) and $E_{0,0}$ is the 0–0 transition energy (approximated from the absorption onset).

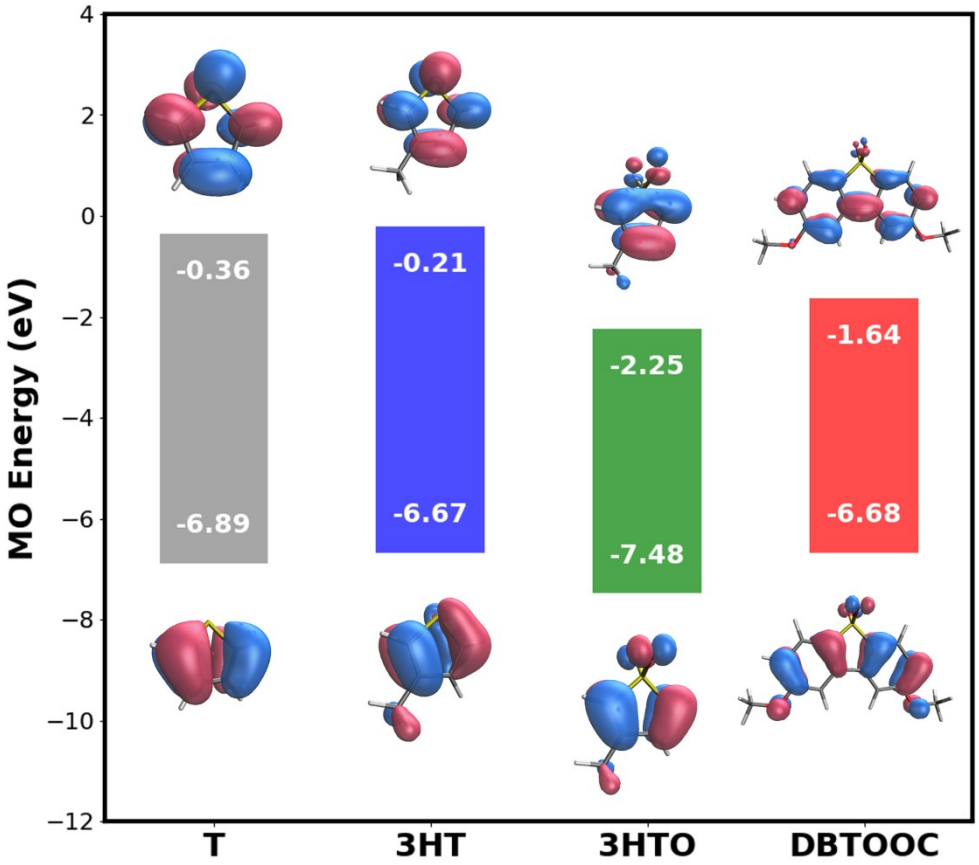

Fig. S19. Energy levels and frontier molecular orbitals of the building blocks.

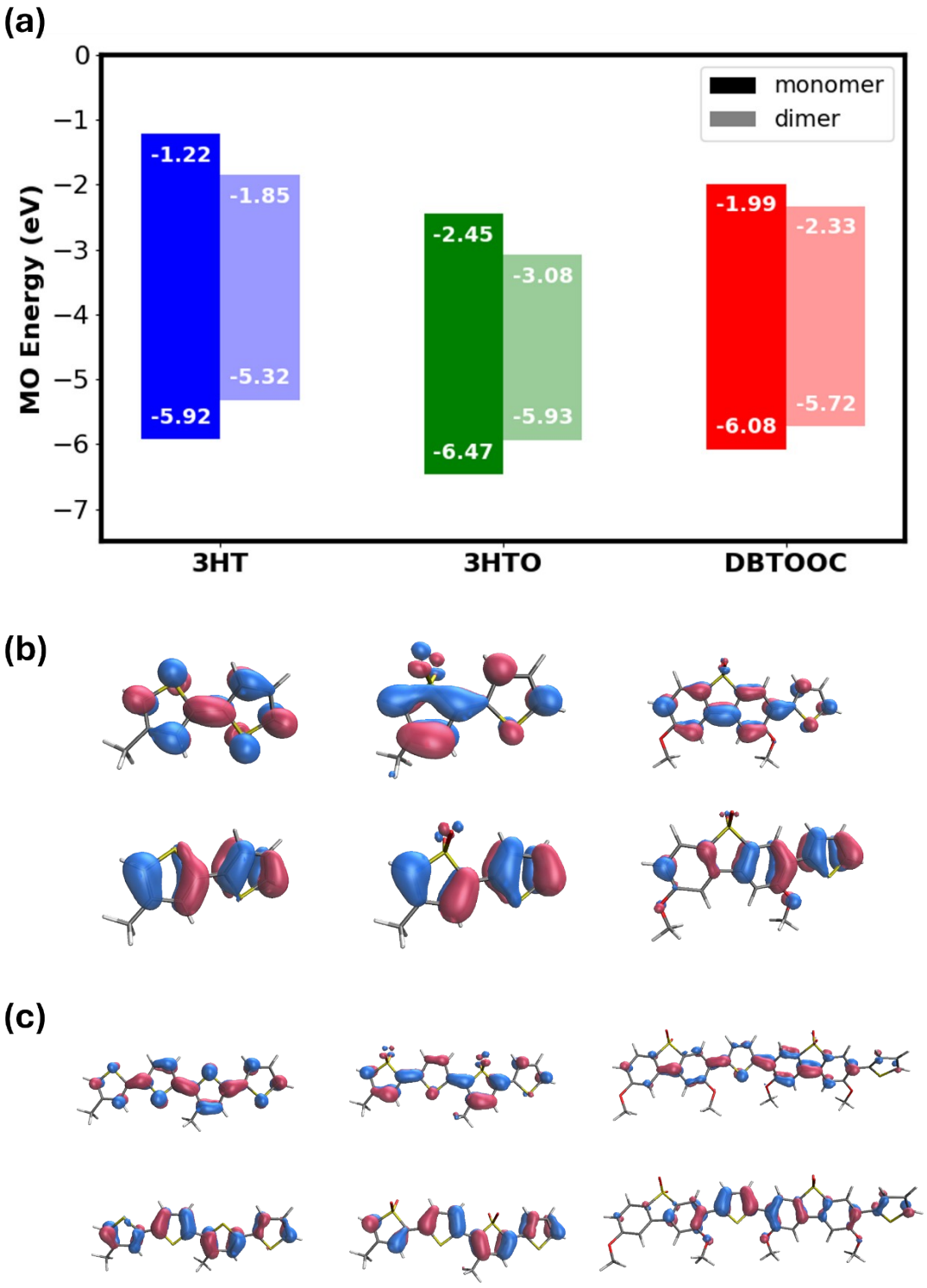

Fig. S20. Energy levels and frontier molecular orbitals of the constituent repeat units. (a) Energy level diagram of monomer (dark) and dimer (light) bars. (b-c) Frontier molecular orbitals (Upper panel: LUMO, Bottom panel: HOMO) for the monomer (b) and dimer (c) units. Both panels show 3HT, 3HTO, and DBTOOC from left to right.

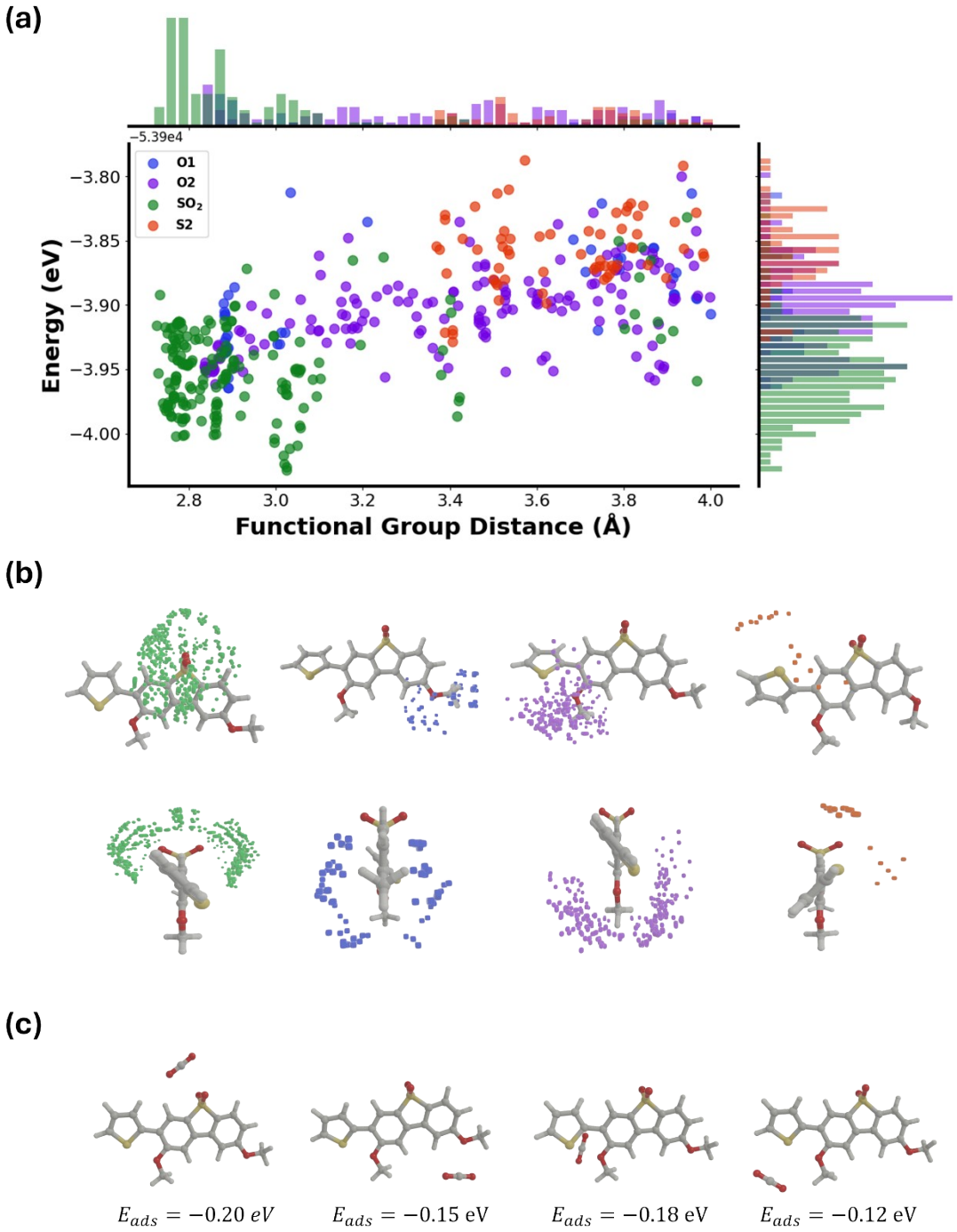

Fig. S21. (a) Conformer search results for CO_2 adsorption near DBTOOC. The right histogram shows the energy distribution of the sampled conformations, and the top histogram shows the distance distribution between CO_2 and the corresponding adsorption functional groups. (b) Spatial distribution of CO_2 for each functional group, with CO_2 center-of-mass positions colored as green (SO_2), blue (O1), purple (O2), and orange (S2). (c) Representative CO_2 physisorption configurations and their adsorption energies (E_{ads}), shown from left to right: SO_2, O1, O2, and S2.

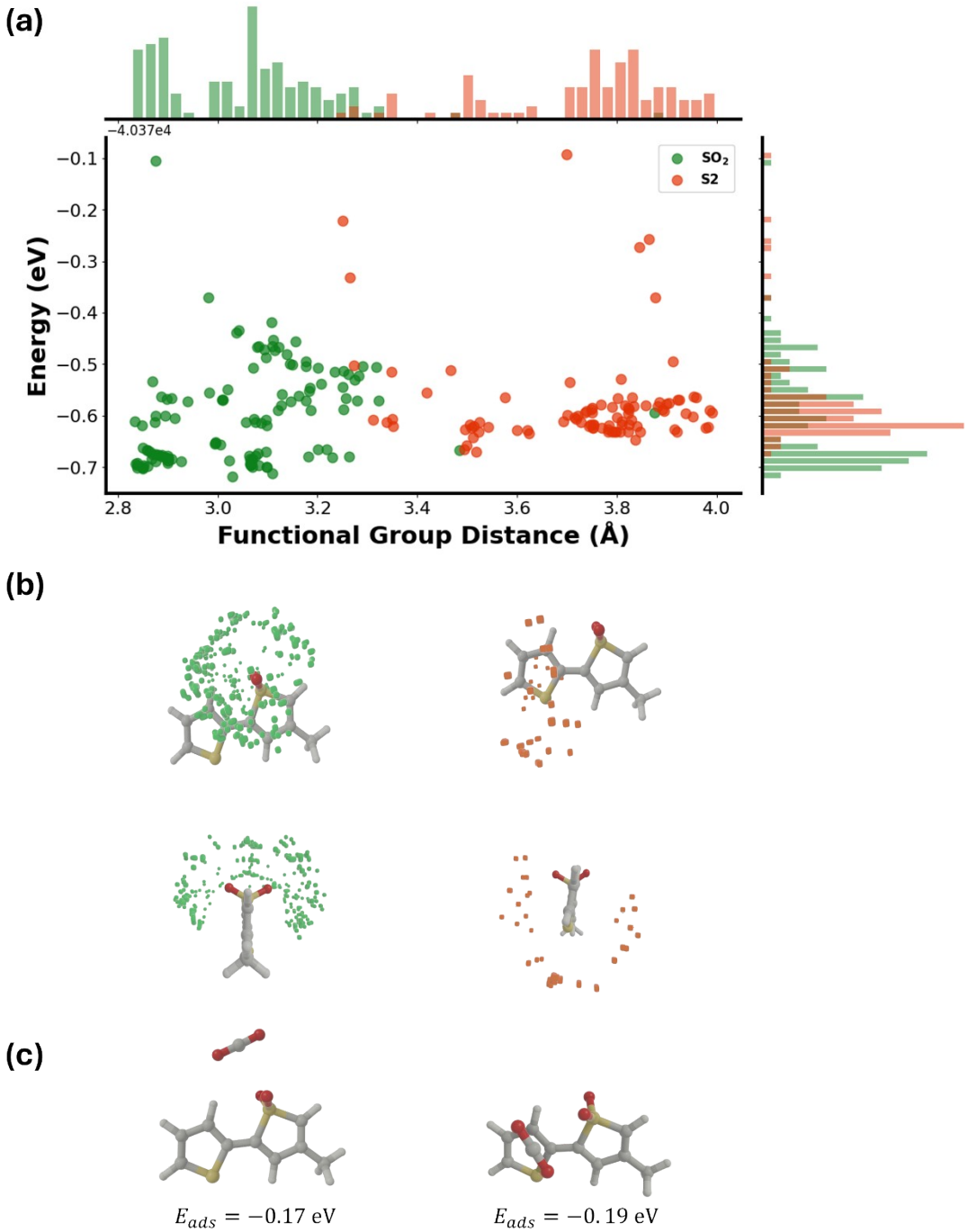

Fig. S22. (a) Conformer search results for CO_2 adsorption near 3HTO. The right histogram shows the energy distribution of the sampled conformations, and the top histogram shows the distance distribution between CO_2 and the corresponding adsorption functional groups. (b) Spatial distribution of CO_2 for each functional group, with CO_2 center-of-mass positions colored as green (SO_2) and orange (S2). (c) Representative CO_2 physisorption configurations and their adsorption energies (E_{ads}), shown from left to right: SO_2 and S2.

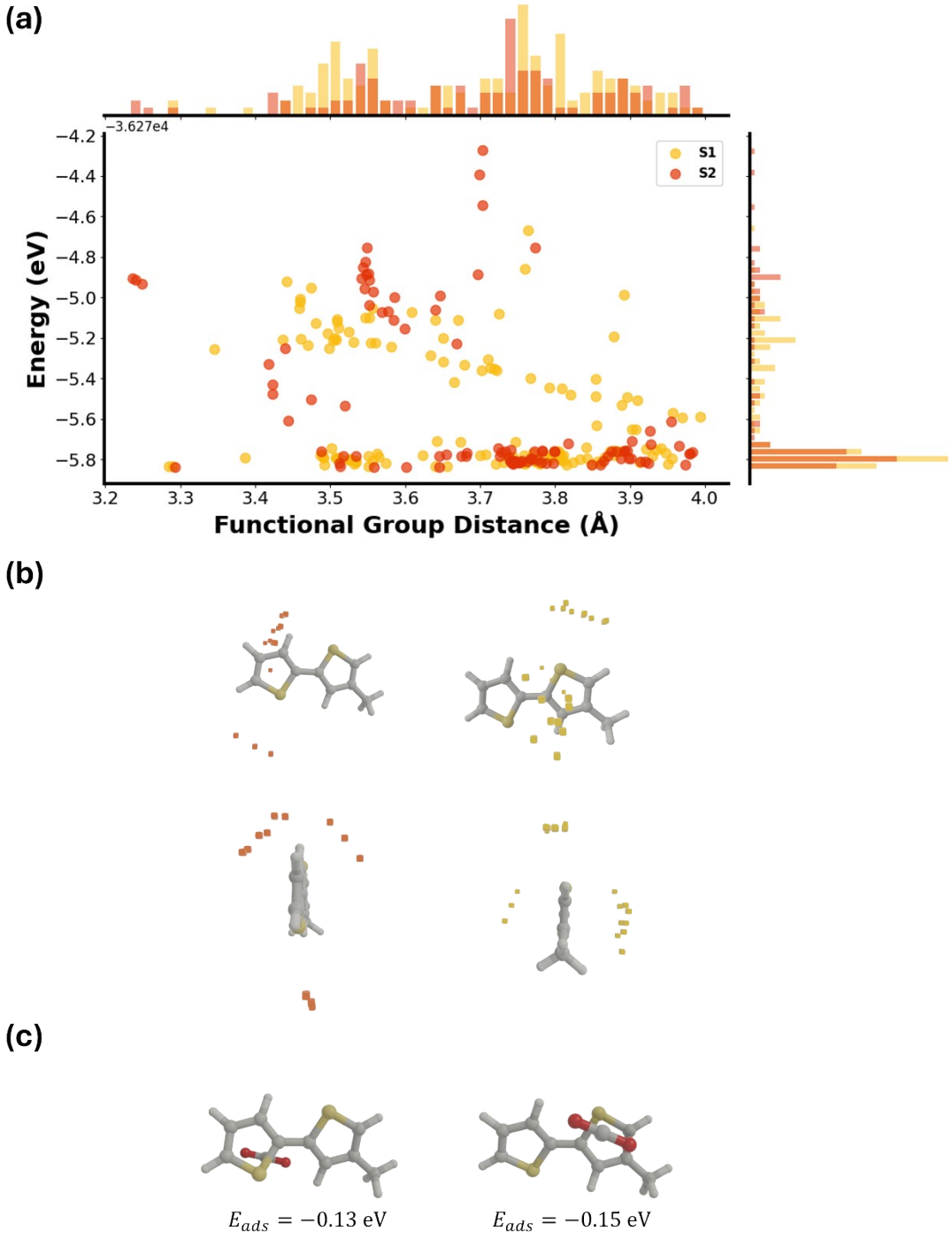

Fig. S23. (a) Conformer search results for CO_2 adsorption near 3HT. The right histogram shows the energy distribution of the sampled conformations, and the top histogram shows the distance distribution between CO_2 and the corresponding adsorption functional groups. (b) Spatial distribution of CO_2 for each functional group, with CO_2 center-of-mass positions colored as yellow (S1), and orange (S2). (c) Representative CO_2 physisorption configurations and their adsorption energies (E_{ads}), shown from left to right: S2 and S1.

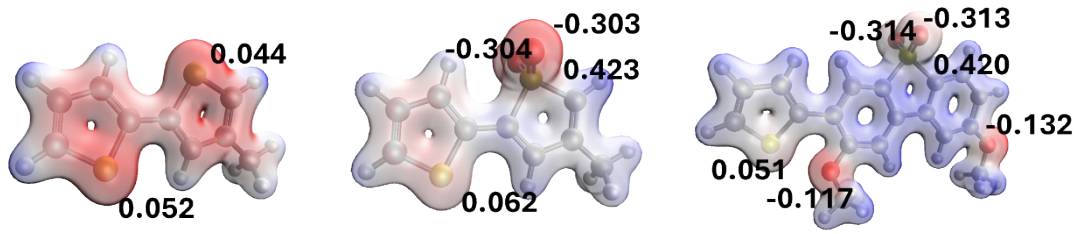

Fig. S24. Electrostatic potential maps of constituent repeat units and Hirshfeld atomic charges of functional group atoms (from left to right: 3HT, 3HTO, and DBTOOC).

Reference

[1] Baerends, E. J.; Aguirre, N. F.; Austin, N. D.; Autschbach, J.; Bickelhaupt, F. M.; Bulo, R.; Cappelli, C.; van Duin, A. C. T.; Egidi, F.; Fonseca Guerra, C.; Förster, A.; Franchini, M.; Goumans, T. P. M.; Heine, T.; Hellström, M.; Jacob, C. R.; Jensen, L.; Krykunov, M.; van Lenthe, E.; Michalak, A.; Mitoraj, M. M.; Neugebauer, J.; Nicu, V. P.; Philipsen, P.; Ramanantoanina, H.; Rüger, R.; Schreckenbach, G.; Stener, M.; Swart, M.; Thijssen, J. M.; Trnka, T.; Visscher, L.; Yakovlev, A.; van Gisbergen, S. The Amsterdam Modeling Suite. *J. Chem. Phys.* **2025**, *162* (16), 162501.

[2] Pracht, P.; Bohle, F.; Grimme, S. Automated Exploration of the Low-Energy Chemical Space with Fast Quantum Chemical Methods. *Phys. Chem. Chem. Phys.* **2020**, *22* (14), 7169–7192.

[3] Anstine, D. M.; Zubatyuk, R.; Isayev, O. AIMNet2: A Neural Network Potential to Meet Your Neutral, Charged, Organic, and Elemental-Organic Needs. *Chem. Sci.* **2025**.

[4] Skånberg, R.; Hotz, I.; Ynnerman, A.; Linares, M. VIAMD: A Software for Visual Interactive Analysis of Molecular Dynamics. *J. Chem. Inf. Model.* **2023**, *63* (23), 7382–7391.

[5] Liang, S.; Huang, L.; Gao, Y.; Wang, Q.; Liu, B. Electrochemical Reduction of CO2 to CO over Transition Metal/N-Doped Carbon Catalysts: The Active Sites and Reaction Mechanism. *Advanced Science* **2021**, *8* (24), 2102886.

[6] Nørskov, J. K.; Bligaard, T.; Logadottir, A.; Kitchin, J. R.; Chen, J. G.; Pandelov, S.; Stimming, U. Trends in the Exchange Current for Hydrogen Evolution. *J. Electrochem. Soc.* **2005**, *152* (3), J23.

References

(S1) Zhu, X.; Yang, N.; Zhou, L.A.; Tian, C.; Wu, J.; Wang, T.; Li, X.; Jiang, X.; Dai, S. Rational Design of Methylated Triazine-Based Linear Conjugated Polymers for Efficient CO_2 Photoreduction with Water. *Advanced Materials*, **2025**, 37(14), p.2417437.

(S2) Zhu, C.; Cheng, J.; Lin, H.; Yang, Z.; Huang, Y.; Lv, F.; Bai, H.; Wang, S. Rational Design of Conjugated Polymers for Photocatalytic CO_2 Reduction: Towards Localized CO Production and Macrophage Polarization. *Journal of the American Chemical Society*, **2024**, 146(36), pp.24832-24841.

(S3) Ye, W.; Wang, Y.; Li, B., Qin, X.; Chen, X.; Zhang, J.; Chen, M.; Zhang, C. Design of Azo-Functionalized DA Conjugated Organic Polymers for Photocatalytic Reduction of Ultra-Low Concentration CO_2. *Applied Catalysis B: Environment and Energy*. **2025**, 125520.

(S4) Wang, S. H.; Khurshid, F.; Chen, P. Z.; Lai, Y. R.; Cai, C. W.; Chung, P. W.; Hayashi, M.; Jeng, R. J.; Rwei, S. P.; Wang, L. Solution-processable Naphthalene Diimide-Based Conjugated Polymers as Organocatalysts for Photocatalytic CO_2 Reaction with Extremely Stable Catalytic Activity for Over 330 Hours. *Chem. Mater.* **2022**, *34*, 4955-4963.

(S5) Wu, W.; Feng, C.; Chen, M.; Tan, Q.; Deng, Y.; Zeng, C.; Zhong, L.; Dai, C. Novel Benzimidazole-Linked Microporous Conjugated Polymers for Highly Selective Adsorption and Photocatalytic Reduction of Diluted CO_2. *Green Chem.* **2023**, *25*, 9335-9342.

(S6) Mohata, S.; Das, R.; Koner, K.; Riyaz, M.; Das, K.; Chakraborty, S.; Ogaeri, Y.; Nishiyama, Y.; C Peter, S.; Banerjee, R. Selective Metal-Free CO_2 Photoreduction in

Water Using Porous Nanostructures with Internal Molecular Free Volume. *J. Am. Chem. Soc.* **2023**, *145*, 23802-23813.

(S7) Aitchison, C. M.; Gonzalez-Carrero, S.; Yao, S.; Benkert, M.; Ding, Z.; Young, N. P.; Willner, B.; Moruzzi, F.; Lin, Y.; Tian, J.; Nellist, P. D. Templated 2D Polymer Heterojunctions for Improved Photocatalytic Hydrogen Production. *Adv. Mater.* **2023**, 2300037.

(S8) He, J.; Wang, X.; Jin, S.; Liu, Z. Q.; Zhu, M. 2D Metal-free Heterostructure of Covalent Triazine Framework/G-C_3N_4 for Enhanced Photocatalytic CO_2 Reduction with High Selectivity. *Chin. J. Catal.*, **2022**, *43*, 1306-1315.

(S9) Yang, C.; Huang, W.; da Silva, L. C.; Zhang, K. A.; Wang, X. Functional Conjugated Polymers for CO_2 Reduction Using Visible Light. *Chem. Eur. J.* **2018**, *24*, 17454-17458.

(S10) Yang, S.; Hu, W.; Zhang, X.; He, P.; Pattengale, B.; Liu, C.; Cendejas, M.; Hermans, I.; Zhang, X.; Zhang, J.; Huang, J. 2D covalent Organic Frameworks as Intrinsic Photocatalysts for Visible Light-Driven CO_2 Reduction. *J. Am. Chem. Soc.* **2018**, *140*, 14614-14618.

(S11) Fu, Y.; Zhu, X.; Huang, L.; Zhang, X.; Zhang, F.; Zhu, W. Azine-based Covalent Organic Frameworks as Metal-Free Visible Light Photocatalysts for CO_2 Reduction with H_2O. *Appl. Catal. B: Environ.* **2018**, *239*, 46-51.

(S12) Lai, W. C.; Wang, S. H.; Sun, H. S.; Liao, C. W.; Liu, T. Y.; Lee, H. T.; Yang, H. R.; Wang, L.; Lai, Y. Y. Stable and Exclusive Formation of CO from CO_2 Photoreduction with H_2O Facilitated by Linear Fluorene and Naphthalene Diimide-Based Conjugated Polymers. *ACS Appl. Polym. Mater.* **2021**, *4*, 521-526.

(S13) Yu, X.; Tian, S.; Zhang, F.; Gao, G.; Zhang, C.; Han, Y.; Ji, S.; Guo, H.; Jin, X. H. Tailoring the Exciton Binding Energy of 2D Conjugated Polymers for Powering Metal-Free CO_2 Photoreduction. *ACS Sustain. Chem. Eng.* **2022**, *10*, 16182-16188.

(S14) Wang, S. H.; Raja, R.; Hsiow, C. Y.; Khurshid, F.; Yang, H. R.; Chung, P. W.; Lai, Y. Y.; Jeng, R. J.; Wang, L. Chromatic Fulleropyrrolidine as Long-Lived Metal-Free Catalyst for CO_2 Photoreduction Reaction. *ChemSusChem* **2022**, *15*, e20210247.

(S15) Dey, A.; Rahimi, F. A.; Barman, S.; Hazra, A.; Maji, T. K. Metal-free 3D Donor–Acceptor COF with Low Exciton Binding for Solar Fuel Production Based On CO_2 Reduction. *J. Mater. Chem. A.* **2023**.

(S16) Yu, X.; Yang, Z.; Qiu, B.; Guo, S.; Yang, P.; Yu, B.; Zhang, H.; Zhao, Y.; Yang, X.; Han, B.; Liu, Z. Eosin Y-Functionalized Conjugated Organic Polymers for Visible-Light-Driven CO_2 Reduction with H_2O to CO with High Efficiency. *Angew. Chem. Int. Ed.* **2019**, *58*, 632-636.

(S17) Ran, L.; Li, Z.; Ran, B.; Cao, J.; Zhao, Y.; Shao, T.; Song, Y.; Leung, M. K.; Sun, L.; Hou, J. Engineering Single-Atom Active Sites on Covalent Organic Frameworks for Boosting CO_2 Photoreduction. *J. Am. Chem. Soc.* **2022**, *144*, 17097-17109.

(S18) Shen, M.; Zhang, L.; Wang, M.; Tian, J.; Jin, X.; Guo, L.; Wang, L.; Shi, J. Carbon-Vacancy Modified Graphitic Carbon Nitride: Enhanced CO_2 Photocatalytic Reduction Performance and Mechanism Probing. *J. Mater. Chem. A.* **2019**, *7*, 1556-1563.

(S19) Hayat, A.; Sohail, M.; Taha, T. A.; Alenad, A. M.; Irfan, A.; Shaishta, N.; Hayat, A.; Mane, S. K. B.; Khan, W. U. A Butterfly Shaped Organic Heterojunction Photocatalyst for Effective Photocatalytic CO_2 Reduction. *CrystEngComm* **2021**, *23*, 4963-4974.

(S20) Aitchison, C. M.; Gonzalez-Carrero, S.; Yao, S.; Benkert, M.; Ding, Z.; Young, N. P.; Willner, B.; Moruzzi, F.; Lin, Y.; Tian, J.; Nellist, P. D. Templated 2D Polymer Heterojunctions for Improved Photocatalytic Hydrogen Production. *Adv. Mater.* **2023**, 2300037.

(S21) Moruzzi, F.; Zhang, W.; Purushothaman, B.; Gonzalez-Carrero, S.; Aitchison, C. M.; Willner, B.; Ceugniet, F.; Lin, Y.; Kosco, J.; Chen, H.; Tian, J. Solution-processable Polymers of Intrinsic Microporosity for Gas-Phase Carbon Dioxide Photoreduction. *Nat. Commun.* **2023**, *14*, 3443.

(S22) Neese, F. The ORCA Program System. *WIREs Computational Molecular Science* **2012**, *2* (1), 73–78.

(S23) Baerends, E. J.; Aguirre, N. F.; Austin, N. D.; Autschbach, J.; Bickelhaupt, F. M.; Bulo, R.; Cappelli, C.; van Duin, A. C. T.; Egidi, F.; Fonseca Guerra, C.; Förster, A.; Franchini, M.; Goumans, T. P. M.; Heine, T.; Hellström, M.; Jacob, C. R.; Jensen, L.; Krykunov, M.; van Lenthe, E.; Michalak, A.; Mitoraj, M. M.; Neugebauer, J.; Nicu, V. P.; Philipsen, P.; Ramanantoanina, H.; Rüger, R.; Schreckenbach, G.; Stener, M.; Swart, M.; Thijssen, J. M.; Trnka, T.; Visscher, L.; Yakovlev, A.; van Gisbergen, S. The Amsterdam Modeling Suite. *J. Chem. Phys.* **2025**, *162* (16), 162501.

(S24) Pracht, P.; Bohle, F.; Grimme, S. Automated Exploration of the Low-Energy Chemical Space with Fast Quantum Chemical Methods. *Phys. Chem. Chem. Phys.* **2020**, *22* (14), 7169–7192.

(S25) Anstine, D.; Zubatyuk, R.; Isayev, O. AIMNet2: A Neural Network Potential to Meet Your Neutral, Charged, Organic, and Elemental-Organic Needs. ChemRxiv October 12, 2023.

(S26) Baerends, E. J.; Aguirre, N. F.; Austin, N. D.; Autschbach, J.; Bickelhaupt, F. M.; Bulo, R.; Cappelli, C.; van Duin, A. C. T.; Egidi, F.; Fonseca Guerra, C.; Förster, A.; Franchini, M.; Goumans, T. P. M.; Heine, T.; Hellström, M.; Jacob, C. R.; Jensen, L.; Krykunov, M.; van Lenthe, E.; Michalak, A.; Mitoraj, M. M.; Neugebauer, J.; Nicu, V. P.; Philipsen, P.; Ramanantoanina, H.; Rüger, R.; Schreckenbach, G.; Stener, M.; Swart, M.; Thijssen, J. M.; Trnka, T.; Visscher, L.; Yakovlev, A.; van Gisbergen, S. The Amsterdam Modeling Suite. *J. Chem. Phys.* **2025**, *162* (16), 162501.

(S27) Pracht, P.; Bohle, F.; Grimme, S. Automated Exploration of the Low-Energy Chemical Space with Fast Quantum Chemical Methods. *Phys. Chem. Chem. Phys.* **2020**, *22* (14), 7169–7192.

(S28) Anstine, D. M.; Zubatyuk, R.; Isayev, O. AIMNet2: A Neural Network Potential to Meet Your Neutral, Charged, Organic, and Elemental-Organic Needs. *Chem. Sci.* **2025**.

(S29) Skånberg, R.; Hotz, I.; Ynnerman, A.; Linares, M. VIAMD: A Software for Visual Interactive Analysis of Molecular Dynamics. *J. Chem. Inf. Model.* **2023**, *63* (23), 7382–7391.

(S30) Liang, S.; Huang, L.; Gao, Y.; Wang, Q.; Liu, B. Electrochemical Reduction of CO2 to CO over Transition Metal/N-Doped Carbon Catalysts: The Active Sites and Reaction Mechanism. *Advanced Science* **2021**, *8* (24), 2102886.

(S31) [Nørskov, J. K.; Bligaard, T.; Logadottir, A.; Kitchin, J. R.; Chen, J. G.; Pandelov, S.; Stimming, U. Trends in the Exchange Current for Hydrogen Evolution. *J. Electrochem. Soc.* **2005**, *152* (3), J23.